AGU PUBLICATIONS

Journal of Advances in Modeling Earth Systems

RESEARCH ARTICLE
10.1002/2017MS000988

Improving the Representation of Polar Snow and Firn in the Community Earth System Model

Leonardus van Kampenhout[1], Jan T. M. Lenaerts[1], William H. Lipscomb[2,3], William J. Sacks[3], David M. Lawrence[3], Andrew G. Slater[4], and Michiel R. van den Broeke[1]

[1]Institute for Marine and Atmospheric Research Utrecht, Utrecht University, Utrecht, The Netherlands, [2]Group T-3, Los Alamos National Laboratory, Los Alamos, NM, USA, [3]National Center for Atmospheric Research, Boulder, CO, USA, [4]National Snow and Ice Data Center, Boulder, CO, USA

Key Points:
- Near-surface snow density modulates heat transport and, indirectly, melt, and should thus be realistically modeled over ice sheets
- New snow physics and parameters show a significant improvement with respect to snow density observations, both at the surface and at depth
- Deep ice temperatures rise by several degrees due to the deepening of the snow pack, and the associated deeper percolation

Supporting Information:
- Supporting Information S1

Correspondence to:
L. van Kampenhout,
L.vankampenhout@uu.nl

Citation:
van Kampenhout, L., Lenaerts, J. T. M., Lipscomb, W. H., Sacks, W. J., Lawrence, D. M., Slater, A. G., & van den Broeke, M. R. (2017). Improving the representation of polar snow and firn in the Community Earth System Model. *Journal of Advances in Modeling Earth Systems*, *9*, 2583–2600. https://doi.org/10.1002/2017MS000988

Received 27 MAR 2017
Accepted 16 OCT 2017
Accepted article online 25 OCT 2017
Published online 16 NOV 2017

Abstract In Earth system models, terrestrial snow is usually modeled by the land surface component. In most cases, these snow models have been developed with an emphasis on seasonal snow. Questions about future sea level rise, however, prompt the need for a realistic representation of perennial snow, as snow processes play a key role in the mass balance of glaciers and ice sheets. Here we enhance realism of modeled polar snow in the Community Land Model (CLM), the land component of the Community Earth System Model (CESM), by implementing (1) new parametrizations for fresh snow density, destructive metamorphism, and compaction by overburden pressure, (2) by allowing for deeper snow packs, and (3) by introducing drifting snow compaction, with a focus on the ice sheet interior. Comparison with Greenlandic and Antarctic snow density observations show that the new physics improve model skill in predicting firn and near-surface density in the absence of melt. Moreover, compensating biases are removed and spurious subsurface melt rates at ice sheets are eliminated. The deeper snow pack enhances refreezing and allows for deeper percolation, raising ice temperatures up to 15°C above the skin temperature.

1. Introduction

The Greenland ice sheet (GrIS) and parts of the Antarctic ice sheet (AIS) are located in the world's fastest warming regions (Masson-Delmotte et al., 2006), and their mass loss is expected to contribute significantly to future sea level rise. The Intergovernmental Panel on Climate Change (IPCC) estimates a global mean sea level rise of 0.28–0.98 m by 2100, of which up to 40% is attributed to ice sheet mass loss (IPCC AR5; Church et al., 2013). Beyond 2100, ice sheet-climate feedbacks start playing a role, especially in high-emission scenarios. For instance, Ridley et al. (2005) showed that changes in ice sheet topography will affect large-scale atmospheric circulation. Also, increasing freshwater fluxes from melting ice and snow could cause shifts in ocean circulation, affecting regional climate (Hu et al., 2009; Lenaerts et al., 2015; Zhu et al., 2014).

To capture these feedbacks, ice sheet models are now being incorporated into Earth system models (ESMs; e.g., Lipscomb et al., 2013; Mikolajewicz et al., 2007; Vizcaíno et al., 2010), and the Ice Sheet Model Intercomparison Project for CMIP6 (ISMIP6) recently defined ice sheet-climate feedbacks as a modeling goal (Nowicki et al., 2016). There are two major challenges involved. The first challenge concerns the difference in scales, both spatially and temporally. A typical ice sheet model has a length scale of 10 km and a long response time—decades to millennia. In contrast, global atmosphere models typically run at a coarser resolution (100 km), yet have comparatively short response times—weeks to months. This difference in scales is addressed by employing asynchronous coupling between ice sheet and climate models (Helsen et al., 2013; Ridley et al., 2005), and by applying upscaling and downscaling techniques to coupling fields. The second challenge concerns realistic coupling fields, usually temperature and surface mass balance (SMB). SMB is commonly defined as the mass flux through the atmosphere/snow interface (precipitation minus sublimation), less runoff from snow and bare ice. Failure to accurately represent SMB results in unrealistic ice sheet geometries (Cullather et al., 2014; Goelzer et al., 2013; Nowicki et al., 2013). Of course, SMB modeling cannot be studied entirely independently from resolution, because of local spatial heterogeneity on scales smaller than the current resolution of atmosphere models. Downscaling techniques exist that attempt to partially remedy this, using subgrid tiling (e.g., Lipscomb et al., 2013).

Another challenge to realistic modeling of ice sheet SMB is the representation of snow and ice melt. Energy balance and vertically resolved snow pack models are known to yield more realistic ablation rates than so-called temperature-index schemes, which are tuned to present-day climates (Bougamont et al., 2007; Pritchard et al., 2008). Additionally, in a warming climate, firn (a term used for snow that has survived at least one season) acts as a buffer delaying the occurrence of meltwater runoff until storage capacity is reached (Machguth et al., 2016; Noël et al., 2017; van Angelen et al., 2013; van Pelt et al., 2016). Obtaining realistic results from an energy balance and snow pack model is challenging because of the many meteorological parameters to which it is sensitive, affecting, e.g., albedo (Rae et al., 2012). Nevertheless, most climate models have implemented detailed snow pack models and found improvements to their SMB simulations (Cullather et al., 2014; Punge et al., 2012; Vizcaíno et al., 2013).

Here we evaluate and improve the representation of snow and firn in the Community Land Model version 4 (CLM4), the terrestrial component of the Community Earth System Model (CESM; Hurrell et al., 2013). Previous work with this model has highlighted problems associated with (1) the limited refreezing capacity in the shallow snow pack (maximum snow depth $H_{max} = 1$ m snow water equivalent (SWE); Vizcaíno et al., 2013) and (2) unrealistic melt rates due to an underestimation of vertical heat transport (Lenaerts et al., 2016). In this study, the representation of polar snow and firn in CESM is improved by changing the fresh snow density and density evolution, and by increasing the maximum depth. We evaluate the changes using a standalone firn densification model with a high vertical resolution, and a set of global CLM simulations forced by atmospheric reanalysis data. For this study, firn density observations are taken from the ice sheet interior, where melt is mostly absent. Follow-up work is planned to evaluate the surface energy and mass balance in the coupled model, including the percolation and ablation zones of the ice sheet. The paper is organized as follows. Section 2 introduces CESM and describes the main characteristics of its terrestrial snow pack model. Changes in model physics are described in section 3 and subsequently evaluated using a firn densification model (section 4). CLM simulation setup and results are discussed in section 5, followed by concluding remarks (section 6).

2. Model Description

CESM is a fully coupled climate model with as principal components the Community Atmosphere Model (CAM; Neale et al., 2010), the Parallel Ocean Program (POP2; Smith et al., 2010), the Community Land Model (CLM; Lawrence et al., 2011), Community Ice CodE (CICE; Hunke et al., 2010) and the Community Ice Sheet Model (CISM; Lipscomb et al., 2013). Energy balance calculations over ice sheets are performed in CLM4, which typically runs at a latitudinal resolution of 1° (∼111 km), i.e., too coarse to accurately capture the steep slopes and other topographic variations found at ice sheet edges. In contrast, CISM runs at a much higher resolution (typically 4 km) but has no energy balance scheme to interact with the atmosphere. To overcome this discrepancy in resolution, the surface energy balance is calculated by CLM at multiple elevations simultaneously, with lapse-rate corrections for temperature and longwave radiation per elevation class. Each elevation class also maintains an independent snow pack state, and as such yields an elevation-dependent SMB. The vertical SMB-profile is subsequently downscaled toward the high resolution ice sheet grid, which is a considerable improvement over just using a single value per CLM grid cell (Vizcaíno et al., 2013). Moreover, the multiple elevation classes approach is computationally cheap, uses the existing CLM4 snow pack model and, importantly, enables the atmosphere to react instantaneously to changes in ice sheet surface, including albedo changes (Lipscomb et al., 2013).

The multilayer snow module in CLM4 originates from the SNTHERM snow model (Jordan, 1991) and has previously been described by Oleson et al. (2010), Lawrence et al. (2011), and Oleson (2013). Here only details relevant to this study are outlined. Variables modeled are snow density, water content, temperature, grain size, and aerosol concentration. Vertical discretization is performed in an Eulerian fashion, where each layer has a prescribed maximum thickness Δz_{max}. Thinner layers are used near the surface where gradients of temperature and grain size are larger; see Table 1. Layers also have a prescribed minimum thickness Δz_{min}. Whenever layer thickness drops below this minimum, e.g., by sublimation or compaction, the layer is merged with a neighbouring layer. In the special case that there are no neighbouring layers, the snow pack becomes virtual, i.e., a single layer is assumed which is no longer modeled explicitly. When a layer grows beyond its prescribed maximum, a downward mass transfer occurs such that Δz_{max} is satisfied. A new layer

Table 1
Minimum and Maximum Layer Thicknesses (Actual, Not SWE) in the CLM4 Snow Model With 5 Layers

		Δz_{max} (m)	
Layer (k)	Δz_{min} (m)	$N = k$	$N > k$
1 (top)	0.010	0.03	0.02
2	0.015	0.07	0.05
3	0.025	0.18	0.11
4	0.055	0.41	0.23
5 (bottom)	0.115		

Note. From Oleson (2013). The maximum layer thickness Δz_{max} depends on whether the current layer (k) is the bottom layer (N), or not. Indicated in the table is $N = 5$, but N may be smaller depending on the conditions.

is created when there are no layers below. To ensure mass conservation, snow density is corrected during these mass transfers. CLM4 uses a five-layer snow model, with a maximum total depth (or *cap*) of 1 m SWE (Oleson, 2013). This translates to about 2.5 m of snow, assuming a bulk snow density of about 400 kg m^{-3}. In contrast, the depth of the Greenland and Antarctic firn layer extends up to hundreds of meters in the coldest locations (van den Broeke, 2008). Glacial ice in CLM4 is modeled as fully saturated, frozen soil (Oleson, 2013). Fifteen ice layers are used that have a combined depth of 42.1 m.

Radiation calculations over snow-covered areas are handled by the Snow, Ice, and Aerosol Radiative (SNICAR) module (Flanner & Zender, 2006). SNICAR implements two-stream radiation transfer theory to calculate shortwave radiation penetration to deeper layers. Albedo is independently calculated for five different wavelengths and is then averaged into two radiation bands for use in CLM: near-infrared and visible light. Aerosol concentrations (soot) as well as grain size are tracked across layers as they affect scattering and absorption. Following the radiation routine, the heat equation is numerically solved for all snow and soil layers, using an implicit method. In turn, hydrological processes are accounted for, including melt, vertical water transport using a tipping bucket method, capillary retention, and refreezing.

The refreezing capacity is determined by three factors: snow depth, thermal capacity ("cold content"), and porosity. No geothermal heat flux is assumed at the bottom of the soil or ice column, thus the thermal state is solely dependent on the skin temperature, divergence of penetrated shortwave radiation, and latent heat released through refreezing. Snow thermal conductivity is calculated following Jordan (1991):

$$\lambda = \lambda_{air} + \left(7.75\times10^{-5}\rho + 1.105\times10^{-6}\rho^2\right)\left(\lambda_{ice} - \lambda_{air}\right), \quad (1)$$

where ρ is the bulk density of snow, $\lambda_{air} = 0.023$ W m^{-1} K^{-1} and $\lambda_{ice} = 2.29$ W m^{-1} K^{-1} the thermal conductivity of air and ice, respectively. The irreducible water content is set to 3.3% of the effective porosity, and any liquid water that cannot be stored in the snow is converted to runoff.

Fractional snow cover is a subgrid parametrization that is used to capture the nonlinear feedback of snow cover on albedo (Oleson, 2013) and surface fluxes (Swenson & Lawrence, 2012).

3. Snow Model Development

In the previous section, we described general characteristics the CLM snow model. Here aspects of the model are presented that were changed or newly introduced, in order to gain a better representation of polar snow and firn. Model changes can be broadly divided into three categories: (1) bug fixes, (2) parameter updates, and (3) introduction of new physics. As we will see, some changes have an opposing effect.

3.1. Snow Pack Depth

We increased the maximum allowed snow depth H_{max} from 1 to 10 m SWE, which seeks a balance between observations of pore close-off depth and practical limitations. In reality, firn depth can exceed 100 m (van den Broeke, 2008), which translates to >60 m SWE assuming a bulk density of about 600 kg m^{-3}. However, allowing for such a deep snow pack to develop in CLM would induce significantly longer spin-up times. For example, a grid point that receives an annual snowfall of 100 mm yr^{-1} requires 100 years of spin-up with $H_{max} = 10$ m SWE, versus 500 years if $H_{max} = 50$ m SWE. Moreover, imperfect meteorological forcing during spin-up may result in permanent snow cover in places that have seasonal snow in reality. Such a spin-up bias is harder to remove when snow depth is greater, because of hysteresis. We acknowledge a modeling error is made when the snow depth is limited to 10 m SWE, but deem this error small compared to other uncertainties. Also, atmosphere-snow pack interaction mainly affects the snow state in the top few meters. Below 10 m depth, the seasonal cycle in temperature is usually small, <1 K (Cullather et al., 2014). The number of snow model layers is increased from 5 to 12, which is a trade-off between vertical resolution (Table 2)

Table 2
New Minimum and Maximum Layer Thicknesses (Actual, Not SWE) in the Extended, 12-Layer Snow Model

		Δz_{max} (m)	
Layer (k)	Δz_{min} (m)	$N = k$	$N > k$
1 (top)	0.010	0.03	0.02
2	0.015	0.07	0.05
3	0.025	0.18	0.11
4	0.055	0.41	0.23
5	0.115	0.88	0.47
6	0.235	1.83	0.95
7	0.475	3.74	1.91
8	0.955	7.57	3.83
9	1.915	15.24	7.67
10	3.835	30.59	15.35
11	7.675	61.30	30.71
12 (bottom)	15.355		

and computational cost. A recursive formula was used to calculate the new layer thicknesses (supporting information S1). The effect of the deeper snow pack will be evaluated in section 5.

3.2. Snow Capping

CLM prescribes a maximum snow depth (or *snow cap*), H_{max}, in order to prevent runaway snow depths. Any mass in excess of the snow cap (either rain or snow) is routed to the river component and ultimately to the ocean. However, the original code had a design flaw in the way in which this cap was maintained: any precipitation that would force $H > H_{max}$ was routed directly to runoff, and snow pack characteristics were not updated (except for grain size). As a result, the top snow layer aged unrealistically and had high density throughout the year, even during snowfall events. The snow capping code has been rewritten to allow the snow pack to refresh from the top. In the new code, any excess mass is removed from the lowest snow layer instead. The phase of the runoff (liquid or solid) is determined based on the phase ratio present in the bottom snow layer (solid runoff is a crude parametrization of ice berg discharge).

3.3. Fresh Snow Density

In the original CLM code, fresh snow or deposition density is parametrized following Anderson (1976). This parametrization is based on density measurements at a high-elevation site in the Rocky Mountains (Alta, UT). We argue that the surface climate at this site is not representative for ice sheets, as ice sheets are generally much colder and more windy than lower latitude mountainous regions. The inadequacy of the fresh snow density parametrization is one of the main reasons for the excessive subsurface melt that was predicted in Antarctica (Lenaerts et al., 2016). With surface densities being predicted as low as 50 kg m^{-3} in cold conditions (Figure 1a), thermal conductivity was also greatly underpredicted (cf., equation (1)). The surface layer then insulates deeper layers from the atmosphere, inhibiting outward heat transport and promoting warming and eventually, subsurface melt. In reality, heat produced in the subsurface is conducted away, both toward and away from the surface. Therefore, improving the fresh snow density parametrization is key to alleviating issues with excessive subsurface melt.

Here fresh snow density is parameterized by introducing a linear wind-dependent density term ρ_w that is added to the temperature term ρ_T, similar to Liston et al. (2007):

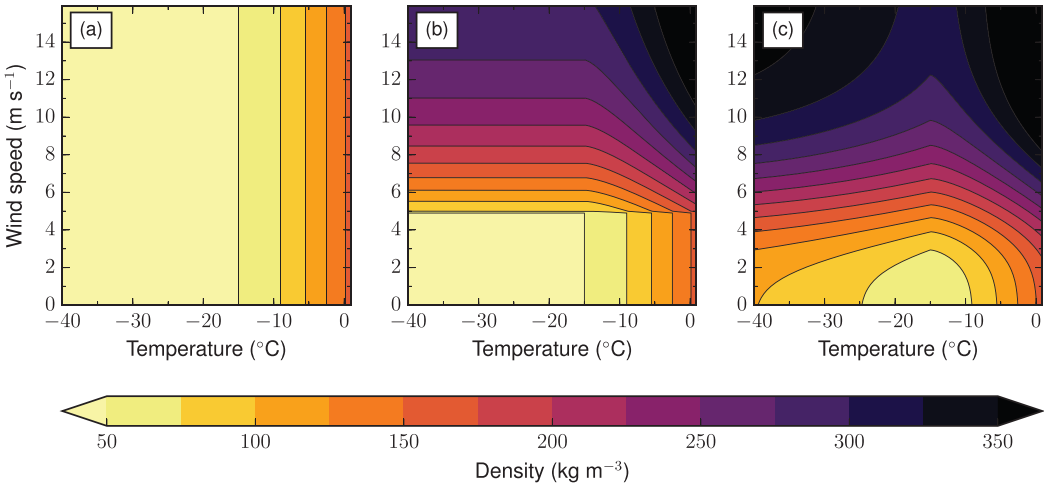

Figure 1. Fresh snow density as a function of temperature and wind speed, (a) the CLM4, temperature-only expression (Anderson, 1976), (b) the same expression, but with an additional wind-dependent term (Liston et al., 2007), and (c) the proposed expression in this paper.

$$\rho_{fs} = \rho_T + \rho_w. \tag{2}$$

This choice is motivated by the fact that strong winds during snowfall cause crystal breaking, thus reducing the snow effective grain size (Sato et al., 2008), which leads to more efficient packing and increased density. Furthermore, snow crystal size depends on temperature, with the smallest particles being found at very low temperatures due to limited moisture availability during crystal formation. Based on unpublished work by A. G. Slater, and assuming ρ in kg m^{-3}, we change the temperature-dependent term to

$$\rho_T = \begin{cases} 50+1.7(17)^{3/2} & \text{if } T > T_{frz}+2, \\ 50+1.7(T-T_{frz}+15)^{3/2} & \text{if } T_{frz}-15 < T \leq T_{frz}+2, \\ -3.8328(T-T_{frz})-0.0333(T-T_{frz})^2 & \text{if } T \leq T_{frz}-15, \end{cases} \tag{3}$$

where T denotes the atmospheric near-surface temperature (in °K), and T_{frz} the freezing temperature of water (273.15°K). Equation (3) predicts a density inversion at very low temperatures, which agrees with observational data (not shown). The wind-dependent term is calculated as follows:

$$\rho_w = 266.861 \times \left(\frac{1}{2}(1+\tanh(U/5))\right)^{8.8}, \tag{4}$$

where U denotes 10 m wind speed in m s^{-1}. The wind-dependent term is based on experimental data and the wind enhancement expression of Liston et al. (2007). The proposed parametrization of fresh snow density (Figure 1c) describes a smooth transition at 5 m s^{-1} wind speed, in contrast to Liston et al. (2007; Figure 1b).

3.4. Snow Densification

Once fallen on the ground, CLM allows snow to densify through three distinct processes: (1) destructive metamorphism, which describes water molecules moving along the snow crystals by sublimation and condensation in order to reduce the surface free energy; (2) compaction by overburden pressure; and (3) melt metamorphism, which captures changes in crystal shape due to the presence and refreezing of liquid water. A fourth process known as constructive metamorphism (Yen, 1981), which relates to temperature gradients and the formation of depth hoar, is not included in CLM. Another limitation of CLM is the absence of microstructural snow properties such as bond size, grain dendricity, and grain sphericity, which are present in more detailed snow pack models like CROCUS (Vionnet et al., 2012) and SNOWPACK (Lehning et al., 2002). Adding these microstructural properties to CLM would require accurate observational constraints, in particular from seasonal snow, and is left to future work.

3.4.1. Destructive Metamorphism

Destructive metamorphism is assumed to be depth independent and has a fixed upper limit. As in the original CLM model, the rate of compaction depends only on temperature (Anderson, 1976):

$$\frac{\partial \rho_i}{\partial t} = c_3 c_2 c_1 \exp\left[-c_4(T_{frz}-T_i)\right], \tag{5}$$

where ρ_i is the bulk density of snow in layer i (excluding liquid water), T_i the layer temperature (K), T_{frz} the freezing temperature of water (273.15 K), $c_3 = 2.777 \times 10^{-6}$ s^{-1}, $c_4 = 0.04$ K^{-1}, c_2 is either 1 or 2 depending on the presence of liquid water, and c_1 is a tapering constant that equals 1 in the range $\rho \in [0, \rho_{max\,DM}]$ and decreases exponentially beyond that. The value of $\rho_{max\,DM} = 175$ kg m^{-3} was chosen heuristically and differs from CLM4, where a value of 100 kg m^{-3} was used (Oleson, 2013). Yen (1981) found that destructive metamorphism is slow when ρ exceeds 250 kg m^{-3}, which supports the current value.

3.4.2. Compaction by Overburden Pressure

Overburden pressure stress causes sintering and mechanical creep and is the dominant force in firn densification. Before, it was modeled following the equations of Anderson (1976):

$$\frac{\partial \rho_i}{\partial t} = \frac{P_i}{\eta_i}, \tag{6}$$

where P_i is the vertical stress or snow load on layer i (in kg m^{-2}) which includes half the weight of the present layer, and η_i is a viscosity coefficient (kg s^{-1} m^{-2}) that varies with density and temperature as

$$\eta = \eta_0 \exp\left[c_5(T_f - T_i) + c_6\rho_i\right], \tag{7}$$

where $\eta_0 = 9\times10^5$ kg s^{-1} m^{-2}, $c_5 = 0.08$ K^{-1}, and $c_6 = 0.023$ m^3 kg^{-1}. Although this parametrization may work well for seasonal snow, it has low skill in predicting polar firn density. In particular, it predicts too strong densification leading to an overestimation of firn density (section 4).

Densification models used for correcting satellite altimetry data over ice sheets typically use empirical compaction schemes, rather than overburden compaction schemes (Kuipers Munneke et al., 2015; Ligtenberg et al., 2011). In principle, an empirical firn densification expression could also be adopted in CLM, but this poses several problems. First, the steady state assumption in empirical models is problematic for most places on Earth where year-to-year climate variability is large, as well as for changing climates. Second, these models require the annual balance rate to be positive, which limits the applicability of the empirical model to glacier accumulation zones. We conclude that a process-based densification model is preferred over an empirical model for global applications, even though it may not perform as well in ice sheet dry snow zones.

The detailed snow model CROCUS also employs overburden pressure compaction (equation (6)), yet defines viscosity differently (Vionnet et al., 2012):

$$\eta = f_1 f_2 \eta_0 \frac{\rho_i}{c_\eta} \exp\left[a_\eta(T_f - T_i) + b_\eta\rho_i\right], \tag{8}$$

where $\eta_0 = 7.62237\times10^6$ kg s^{-1} m^{-2}, $a_\eta = 0.1$ K^{-1}, $b_\eta = 0.023$ m^3 kg^{-1}, and $c_\eta = 250$ kg m^{-3}. f_1 and f_2 are correction factors to snow viscosity that account for the presence of liquid water (f_1) and angular grains (f_2). Here we adopt this expression with two changes: (1) we fix $f_2 = 4.0$, which removes the dependency on grain size, assuming relatively large grains (340 μm or more) and (2) we set $c_\eta = 358$ kg m^{-3} to give a better agreement with firn core data (section 4).

3.5. Compaction by Drifting Snow

Drifting snow is associated with redistribution of surface snow, enhanced sublimation, and crystal breakage. Unfortunately, explicit modeling of redistribution is impractical, due to the large typical length scales in CLM (Lenaerts & van den Broeke, 2012). Here we only introduce the effect of drifting snow on snow compaction at the surface, where crystal breakage is known to lead to more efficient packing, and therefore higher surface densities (Brun et al., 1997).

The compaction effect of drifting snow is included in a simple, parameterized way, following Vionnet et al. (2012) who build on experimental work by Guyomarc'h and Mérindol (1998). We define a mobility index M_O that describes the potential for snow erosion for a given snow layer, assuming nondendritic snow:

$$M_O = 0.34(-0.583g_s - 0.833s + 0.833) + 0.66F(\rho). \tag{9}$$

We assume a constant grain size ($g_s = 0.35$ mm) and spherical grains ($s = 1$), which leads to the following simplification:

$$M_O = -0.069 + 0.66F(\rho). \tag{10}$$

$F(\rho)$ denotes a density-dependent term and is computed as $F(\rho) = [1.25 - 0.0042(\max(\rho_{\min}, \rho) - \rho_{\min})]$ with $\rho_{\min} = 50$ kg m^{-3}. The value of F ranges between 0.2 for consolidated snow ($\rho = 300$ kg m^{-3}) to over 1.0 for low-density snow ($\rho = 100$ kg m^{-3} or less). We conclude that the mobility index is dominated by the density-dependent term, even if we would allow for varying dendricity and sphericity (low sphericities are typical of fresh snow, having a low density), which implies that the error introduced by assuming nondendritic, spherical snow is acceptable.

The mobility index is combined with wind speed to compute the driftability index:

$$S_I = -2.868\exp(-0.085U) + 1 + M_O, \tag{11}$$

where positive values of S_I indicate that drifting snow occurs (Vionnet et al., 2012). As we assume constant snow grain properties, only snow density is affected by drifting snow events:

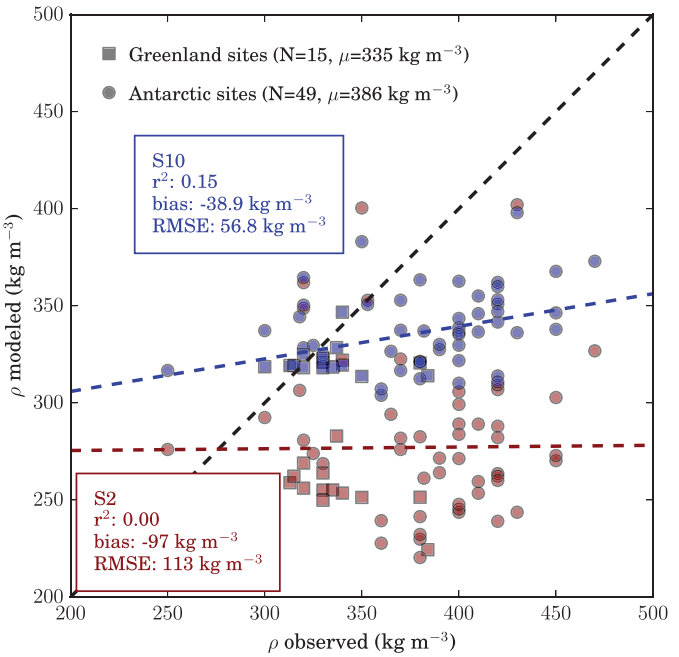

Figure 2. Average near-surface density in observations and model experiments. S2 has the original CLM4 expressions for fresh snow density and densification, whereas S10 contains the improvements described in the text (Table 3).

$$\frac{\partial \rho_i}{\partial t} = \frac{\rho_{\max} - \rho}{\tau_i}, \tag{12}$$

with upper limit $\rho_{\max} = 350$ kg m^{-3} and τ_i the characteristic timescale dependent on the driftability index:

$$\tau_i = \frac{\tau}{\Gamma^i_{\text{drift}}} \quad , \quad \Gamma^i_{\text{drift}} = \max\left[0, S^i_{\text{I}} \exp\left(-z_i/0.1\right)\right]. \tag{13}$$

The upper limit $\rho_{\max}$ to which drifting snow compaction is active is based on observations on both ice sheets (Figure 2 and Groot Zwaaftink et al., 2013). The characteristic time scale for drifting snow compaction τ is empirically set to 48 h, and the pseudo-depth z_i takes into account previous hardening of snow layers above the current layer: $z_i = \sum_j D_j \cdot (3.25 - S^j_{\text{I}})$, with D_j being the layer thickness (Vionnet et al., 2012).

4. Evaluation of Code Changes in Absence of Melt

In the absence of melt, snow compaction is solely driven by the mechanisms that were just described. So in order to justify the physical changes made, we ran a number of simulations using an offline dry firn densification model and compared these to observational data.

4.1. Model Description, Data, and Methods

The processes presented in section 3 have been implemented in a single-column numerical model that couples the heat equation to snow compaction and snow metamorphism laws. This simple model allows for quick development and efficient simulations with greater vertical detail than is possible in CLM. At the surface, the model is forced with high-frequency meteorological data: skin temperature (applied as a Dirichlet boundary condition), SMB, and 10 m wind speed. No heat transport is allowed through the bottom of the column (Neumann boundary condition), which is a valid assumption when the deep snow pack is isothermal at the mean annual surface temperature (Li & Zwally, 2004). No trend in surface temperature is assumed. The heat equation is solved using Crank-Nicholson implicit time discretization and a tridiagonal solver (LAPACK dgtsv). Thermal conductivity is parameterized according to equation (1). The model does not simulate hydrological processes, which limits its applicability to locations where melt is absent or marginal, i.e., interior Antarctica and Greenland. Six-hourly meteorological forcing is used from the regional climate model RACMO version 2.3 for the reference periods 1957–2000 (GrIS; Noël et al., 2015) and 1979–2013 (AIS; Van Wessem et al., 2014). During the spin-up, meteorological forcing is looped until an approximate equilibrium is reached, measured in terms of temperature and density.

Model experiments at 89 sites have been performed, and results are compared to in situ measurements (snow pits and firn cores). Observational sites are divided into 53 Antarctic sites (Fernandoy et al., 2010; Graf & Oerter, 2006; Oerter et al., 2000; van den Broeke, 2008; Wagenbach et al., 1994) and 36 Greenland sites (Benson, 1962; Kuipers Munneke et al., 2015; Morris & Wingham, 2011; Mosley-Thompson et al., 2001). On Greenland, we only selected firn cores that see little to no melt, i.e., where the ratio of melt to accumulation is less than or equal to 0.02).

Two metrics are used to evaluate each experiment. The first is the depth of the $\rho = 550$ kg m^{-3} density level ($z550$ hereafter) as a proxy for the transition from settling to sintering as the dominant process in the upper firn compaction. $z550$ is commonly used to evaluate firn compaction models (e.g., Ligtenberg et al., 2011). The second metric is near-surface density, a quantity that is notoriously difficult to constrain from observations, for several reasons. First, large heterogeneities may exist horizontally due to redistribution and differences in atmospheric forcing. Second, low-density layers on top of consolidated snow have been observed, which make surface density an ambiguous concept (Brun et al., 2011). Finally, snow density measurements are sparse and performed at different depths, from several centimeters up to half a meter or more. In this study, we will distinguish between *skin density* ρ_{skin}, the density of the upper model layer, and *near-surface*

Table 3
Overview of Numerical Experiments With the Dry Firn Densification Model, and Selected Results

					$\overline{\rho_{1m}}$			$z550$		
Name	FSD	ρ_{max}^{DM} (kg m^{-3})	Compaction	Drift	r^2	Bias (kg m^{-3})	RMSE (kg m^{-3})	r^2	Bias (m)	RMSE (m)
S1	Helsen08		Herron80	No	0.12	51.8	69.0	0.66	−0.22	2.56
S2	Anderson76	100	Anderson76	No	0.0	−97	113	0.03	−7.59	8.6
S3	Anderson76	100	Herron80	No	0.0	−177	184	0.56	10.5	10.9
S4	Anderson76	175	Herron80	No	0.0	−88	101	0.52	3.66	4.65
S5	This paper	100	Herron80	No	0.39	−103	109	0.64	8.53	8.91
S6	This paper	175	Herron80	No	0.13	−53.7	68.0	0.55	3.52	4.49
S7	This paper	100	Herron80	Yes	0.44	−88.4	94.5	0.68	7.72	8.08
S8	This paper	175	Herron80	Yes	0.21	−49.4	63.7	0.57	3.43	4.4
S9	This paper	175	Vionnet12	Yes	0.16	−42	58.8	0.15	2.28	5.09
S10	This paper	175	This paper	Yes	0.15	−38.9	56.8	0.15	0.0	4.21

Note. Columns from left to right: experiment name; fresh snow density (FSD) parametrization; upper limit for destructive metamorphism; overburden compaction scheme; drifting snow compaction; coefficient of determination r^2, bias and root mean square error for both near-surface density and the depth of the $\rho = 550$ kg m^{-3} density level, with respect to observations at 89 ice sheet sites (see text). Abbreviated references are Helsen2008 (Helsen et al., 2008), Herron80 (Herron & Langway, 1980), Anderson76 (Anderson, 1976), and Vionnet12 (Vionnet et al., 2012).

density $\overline{\rho_{1m}}$, which represents the average snow pack density in the upper meter. Both these quantities are averaged over a climatological period (set to 30 years) to filter out seasonal differences. This means they incorporate ageing and compaction effects and therefore, both these quantities will differ significantly from the deposition density.

Modeled values of $\overline{\rho_{1m}}$ are compared to snow pit and firn core observations at varying depth and time. As such, there is a mismatch both in time (climatological mean versus single measurement) and space (grid cell average versus point measurement), which adds uncertainty. For data records that have more than one sample in the upper first meter, we selected the node depth closest to 0.5 m. Not all measurement sites had recordings of both metrics of interest. The mean observed $z550$ over the 56 available measurements is 11.7 m. The mean observed $\overline{\rho_{1m}}$ over the 64 available measurements is 374 kg m^{-3}. Table 3 lists the different experiments and their performance on the two metrics. The goal of these experiments is to allow for understanding the processes that control near-surface density and firn density, and describe the steps that were taken in order to at least qualitatively match observations. Uncertainties arise from the RACMO2 forcing data used, measuring errors in the firn core data, sparsity of in situ data, and a possible summer bias in the measurements. The good fit of observed firn density profiles with semiempirical steady state firn densification models suggests that the steady state assumption (constant accumulation and temperature) is reasonable for the selected forcing (RACMO).

4.2. Results and Discussion

The first experiment in Table 3, S1, is best regarded as a benchmark experiment for $z550$. Instead of a prognostic equation for overburden compaction, it employs the empirical, steady state firn model of Herron and Langway (1980), which involves the local mass balance rate. Recent work improved upon the steady state parametrization by Herron and Langway (1980) resulting in better fits over the GrIS (Li & Zwally, 2004), AIS (Helsen et al., 2008; Ligtenberg et al., 2011), and coastal Antarctica (Arthern et al., 2010) using new observational data and introducing temperature-dependent activation energies. Since our interest here lies in using S1 as a benchmark experiment, and Herron and Langway (1980) is not tuned toward one ice sheet in particular, this expression is deemed fit-for-purpose. Fresh snow density is set according to the empirical relation by Helsen et al. (2008), which, in fact, was developed as a parametrization for $\overline{\rho_{1m}}$. Therefore, we must realize that a modeling error is introduced by using Helsen et al. (2008) as a predictor for deposition density. This is reflected by the overprediction of $\overline{\rho_{1m}}$ by 51.8 kg m^{-3}. Also, this error may have contributed to the small underprediction of $z550$ by 0.22 m. What is more, the expression by Helsen et al. (2008) contains a slope correction for the AIS. On account of that, we expect model skill in predicting GrIS $z550$ to be worse than AIS $z550$. Indeed, the fit is considerably better at Antarctic sites (r^2=0.78) than at Greenland sites (r^2=0.22). Combined, the predictive skill is fair (r^2=0.66).

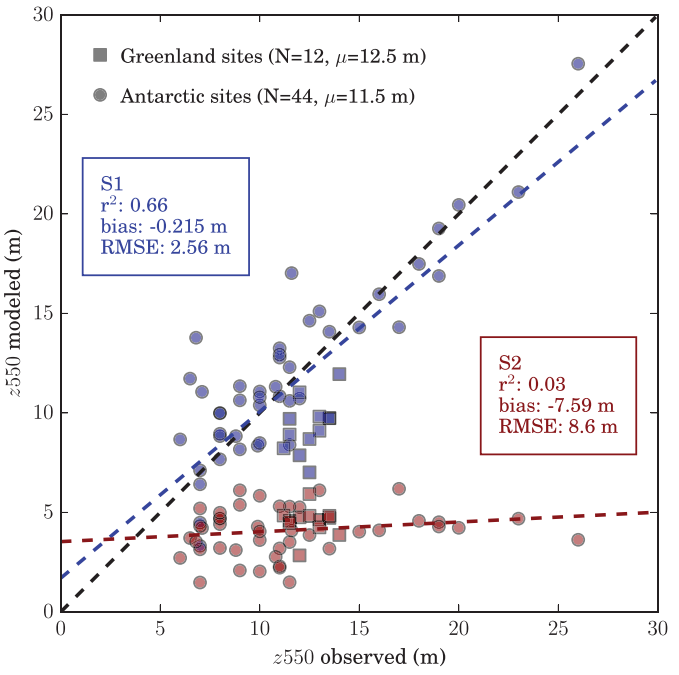

Figure 3. Depth of the $\rho = 550$ kg m^{-3} density level in observations and model experiments. S1 uses empirical expressions for fresh snow density and overburden densification, whereas S2 uses prognostic expressions for those processes, as originally present in CLM4 (Table 3).

S2 uses the original CLM4 pressure compaction and fresh snow density formulations (Anderson, 1976). By intercomparing S2 and S1 we get a sense of how much skill CLM has in resolving firn density. Unfortunately, we find that it is rather inadequate in resolving the basic ice sheet snow properties that were selected (Table 3). Near-surface density $\overline{\rho_{1m}}$ is substantially underestimated (Figure 2), which is attributed to the absence of key model physics, of which wind-dependent fresh snow density is deemed the most important. The depth of $\rho = 550$ kg m^{-3} is much closer to the surface than in the observations (Figure 3). Indeed, no 550 kg m^{-3} value is found deeper than 7 m. Somewhat surprisingly, the biases in $\overline{\rho_{1m}}$ and $z550$ are of opposing sign: one would expect a negative bias in $\overline{\rho_{1m}}$ coinciding with deeper $z550$, which is not the case here. We attribute this to the overburden compaction scheme, which predicts exceptionally high compaction rates, thus compensating the underestimation of $\overline{\rho_{1m}}$. This effect is clearly observed when plotting the density profile for a particular site (Figure 4).

To separate the effect of fresh snow density and overburden compaction, we conducted a series of sensitivity experiments assuming the steady state Herron and Langway (1980) compaction model as the best estimate expression for firn compaction with depth. This setup allowed us to evaluate the effect of fresh snow density, destructive metamorphism, and drifting snow compaction. First, the unaltered CLM expressions for metamorphism and fresh snow density are combined with the steady state model (experiment S3). Our hypothesis is that because S3 sees lower, more realistic compaction rates than S2, it should predict deeper $z550$ and probably also a decrease in $\overline{\rho_{1m}}$ (because $\overline{\rho_{1m}}$ is a depth-integrated quantity). Indeed, both effects are apparent (Table 3): $z550$ changes from being underestimated to being overestimated (bias: 10.5 m), and the negative bias in $\overline{\rho_{1m}}$ increases to -177 kg m^{-3}. In other words, when a compensating bias is removed, a strong underestimation in $\overline{\rho_{1m}}$ is revealed.

Second, experiment S4 shows that a higher upper limit for destructive metamorphism is beneficial to the simulation of $\overline{\rho_{1m}}$; compared to the S3 experiment, the bias is halved. However, both S3 and S4 show no predictive skill in $\overline{\rho_{1m}}$, as wind speed is not taken into account. We conclude that new physics are needed to get a better simulation of near-surface density.

This is attempted in experiment S5, where the newly developed fresh snow density parametrization is used (equations (3) and (4)), with wind speed dependence. Finally, near-surface density is predicted with some skill (r^2=0.39), yet having a large bias (–103 kg m^{-3}). Like before, this bias is reduced by increasing $\rho_{\max^{\mathrm{DM}}}$, in experiment S6. Compared to simulation S4, there is just a slight improvement in $z550$ modeling skill in S6. We conclude that the newly developed fresh snow density expression greatly improves the model performance, especially in near-surface density.

More new physics are introduced in experiment S7 and S8 that have active drifting snow compaction (section 3.5). Compared to runs with the same $\rho^{\mathrm{DM}}_{\max}$, S5 and S6, we observe small increases in predictive skill and reduced biases for both metrics. This favors inclusion of drifting snow compaction into the model. Its effect is probably not crucial, yet it may be important in special cases, e.g., when deposition density is low. Another argument to include drifting snow is that it is an actual, observed phenomenon. Similar to what we found previously, the increase of $\rho_{\max^{\mathrm{DM}}}$ from 100 to 175 kg m^{-3} reduces predictive skill in favor of improved RMSE and bias.

Experiment S9 replaces the Herron and Langway (1980) steady state firn model by a prognostic pressure compaction expression (Vionnet et al., 2012). The motivation to why (Herron & Langway, 1980) is unfit for use in a ESM is given in section 3.4.2. Although S9 captures the mean $z550$ reasonably well (bias: -2.28 m), there is still a sizable spread (r^2=0.15). In experiment S10, one of the viscosity parameters has been modified (section 3.4.2) in order to remove the remaining $z550$ bias. Unfortunately, this does not improve the

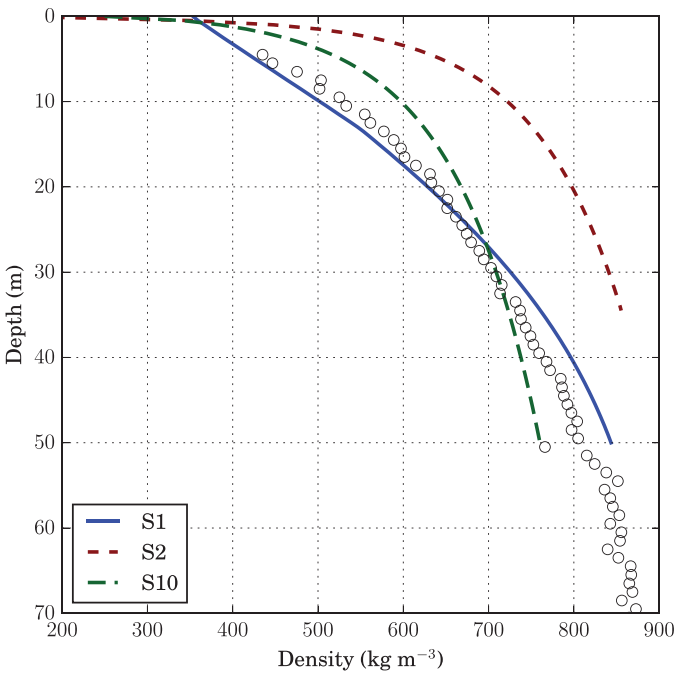

Figure 4. Mean density profiles for the period 1979–2011 as calculated by a single-column densification model, compared to firn core data (Lamorey, 2003) at Siple Dome, Antarctica. Solid lines correspond to the Herron and Langway (1980) empirical model (experiment S1 in Table 3), the original CLM4 overburden pressure compaction scheme (S2), and the modified Vionnet et al. (2012) overburden pressure compaction scheme (S10). Mean forcing accumulation and temperature at this site equal 57.9 mm yr^{-1} and 243°K, respectively.

spread, yet RMSE decreases by almost 1 m. We conclude that the subtle interplay of temperature, wind and SMB remains a great challenge to the overburden pressure scheme.

On balance, the settings in experiment S10 yield an improved simulation of polar snow with respect the the old physics in experiment S2. A compensating bias in $\overline{\rho_{1m}}$ has been identified and resolved, and model skill has improved in this metric. The depth of $\rho = 550$ kg m^{-3} is now better predicted, although a fairly large spread remains (Figure 5). The settings in S10 have been implemented in CLM and will be standard in the next release of the model.

5. Evaluation in CESM

5.1. Data and Methods

Next, three global, land-only (CLM) simulations are performed that show the impact of the deeper snow pack ($H_{max} = 10$ m) and new snow physics on melt and refreezing. Fixed meteorological forcing was chosen in favor of coupled atmosphere-land because of simplicity and computational cost. Meteorological forcing is taken from ERA-Interim reanalysis data (Dee et al., 2011) spanning the years 1979–1998, a period with good satellite coverage and relatively little climate change, at a resolution of approximately 80 km (T255 spectral), upscaled to the ∼1° longitude-latitude CLM grid. The forcing frequency is 6-hourly. Precipitation is assumed solid when $T < T_{frz}$, with T the temperature in the lowest available output layer, and T_{frz} the water freezing point (0°C). Precipitation is assumed liquid above 2°C, and a ramped fraction method is used between 0 and 2°C. On the East Antarctic Plateau, the simulated sublimation flux turned out to outweigh ERA-Interim snowfall, resulting in a negative SMB and bare ice exposure. Underestimation of snowfall in interior East Antarctica was previously reported by Bromwich et al. (2011). This anomaly has been corrected by the application of a scaling factor to the precipitation field, which imposes a lower bound on annual accumulation of 20 mm yr^{-1}, a number supported by observations (Arthern et al., 2006).

Three spin-up simulations have been performed, one for each transient simulation. At the beginning of the spin-ups, ice temperatures over the glaciers and ice sheets were set to the annual average ERA-Interim surface temperature. Meteorological forcing over the period 1979–1998 was looped until deep temperature reaches a quasi-equilibrium, when the maximum absolute difference of deep ice temperature over two consecutive decades did not exceed 1°K. Following this procedure, ERAI-NEW-10m required 120 years of spin-up, whereas the other runs needed 80 years to equilibrate. We assumed that the snow pack is in steady state after this spin-up period. This assumption is not valid for very dry locations, where the firn has not been fully developed, but the departure from steady state is deemed insignificant.

The three spin-up simulations were used to initialize three transient experiments (Table 4). The reference simulation ERAI-OLD-1m uses the basic snow physics of CLM4 (Oleson, 2013), but other code is not identical to CLM4, e.g., the new snow capping scheme is used (section 3.2). The second experiment ERAI-NEW-1m incorporates all the model changes described in section 3, except that it still uses the shallow snow pack $H_{max} = 1$ m. Finally, "firn" simulation ERAI-NEW-10m has $H_{max} = 10$ m.

5.2. Results and Discussion

Figure 6 shows the mean annual surface density, for both ice sheets. Average density over the top 2 cm (ρ_{skin}) is shown, a depth at which overburden pressure compaction is virtually inactive. We find that in the GrIS interior, where previously ρ_{skin} did not exceed 100 kg m^{-3}, surface density now ranges from 250 to 300 kg m^{-3}. This is interpreted as the effect of the newly introduced fresh snow density parametrization, as well as the increased active range of destructive metamorphism (ρ_{max}^{DM}=175 kg m^{-3}), and drifting snow

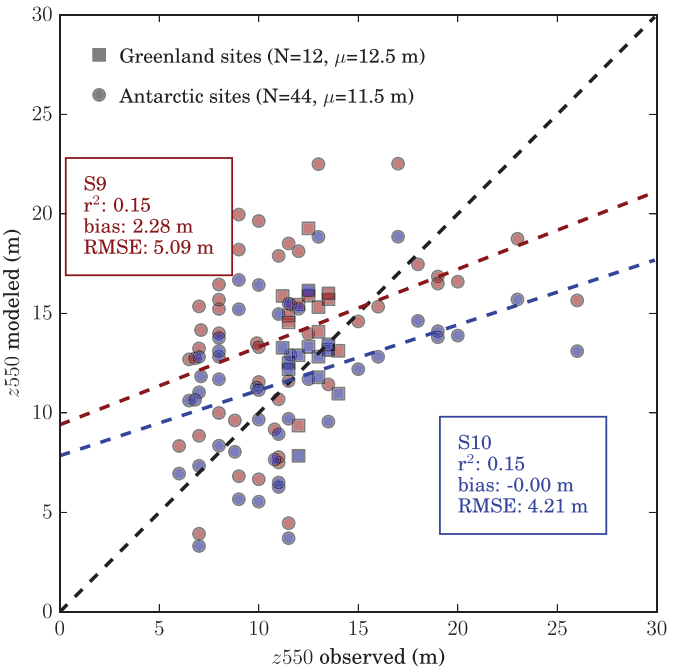

Figure 5. Depth of the $\rho = 550$ kg m^{-3} density level in observations and model experiments. Both S9 and S10 use the new fresh snow density expression and $\rho_{\max}{}^{\mathrm{DM}}$, however differ in their calculation of viscosity (Table 3).

compaction. Given enough exposure time, drifting snow compaction drives any snow density up to a maximum of 350 kg m^{-3} (section 3.5) in windy conditions. At lower elevations, however, drifting snow compaction is counterbalanced by fresh snowfall, resulting in lower densities at the GrIS margin. Strong katabatic winds in the escarpment zone of the East Antarctica ice sheet generate high ρ_{skin} values. Lower surface densities on the Ross and Filchner-Ronne ice shelves are explained by the weaker winds in these regions.

The low surface densities simulated in the ERAI-OLD-1m experiment have a dramatic impact on melt rates. We find that due to excessive melt, large parts of the northern GrIS fail to sustain a permanent snow cover, i.e., SMB < 0 (Figure 6, dashed areas). On Antarctica, bare ice is found across the entire Amery ice shelf. This unrealistic behaviour is largely resolved in experiment ERAI-NEW-1m. With the new model physics, annual GrIS melt volume is reduced by 72% and AIS melt volume by as much as 88% (Table 5).

To study this in more detail, we analyzed the vertical distribution of melt in the snow pack. As mentioned earlier, the SNICAR radiation scheme includes radiation penetration allowing for subsurface melt. With low snow densities, subsurface heat conduction is inhibited. There is neither much conduction toward the surface, where heat may be emitted through black body radiation, nor down toward the cold glacial ice. Heat is thus trapped by the insulating properties of the snow, increasing the chances of bringing temperature to the melting point. Subsurface radiation, accounting for only a small fraction of total absorbed solar radiation (Figure 7), is therefore responsible for the majority of melt in the column (Figure 8). The relationship between density and thermal conductivity is quadratic, meaning that this effect becomes increasingly weaker at higher densities (cf., equation (1)). Still, subsurface melt is the dominant form of melt in simulations ERA-NEW-1m and ERAI-NEW-10m (Figure 8), but the relative importance decreases from 96% to 61% on the AIS, and from 89% to 59% on the GrIS (ERAI-NEW-1m). Note that there is a slight drop in subsurface radiation absorption with increasing density (Figure 7). This is explained by the indirect effect that melt and refreezing have on grain size. Average grain size in simulation ERAI-NEW-1m is 1.5X to 2X smaller than in ERAI-OLD-1m (not shown), due to a combination of (1) reduced presence of liquid water and (2) a drop in refreezing volume (Table 5). Both these processes reduce grain growth (Oleson et al., 2008) and therefore lead to a decrease in absorption. Clearly, these effects outweigh the density dependence of grain size ageing, an opposing effect where denser snow is associated with larger grains and more absorption (Lawrence et al., 2011). Idealized experiments would be needed to quantify the relative importance of each of these effects, which is left to future work. Overall, integrated melt over Greenland is now underestimated with respect to regional climate model results (Table 5). We attribute this to (1) substantial underprediction of solar radiation in the ERA-Interim product (not shown) and (2) remaining model biases that relate to snow melt, e.g., initial grain size, irreducible water content, and soot deposition (van

Table 4
Model Parameters Used in Three Transient Land-Only Simulations

Name	N_s	$H_{\max}$ (m)	Fresh snow density	$\rho_{\max}^{\mathrm{DM}}$ (kg m^{-3})	Compaction	Drift
ERAI-OLD-1m	5	1	Anderson76	100	Anderson76	No
ERAI-NEW-1m	5	1	This paper	175	This paper	Yes
ERAI-NEW-10m	12	10	This paper	175	This paper	Yes

Note. Columns from left to right: experiment name; N_s number of snow layers; $H_{\max}$ maximum snow depth; fresh snow density parametrization; upper limit for destructive metamorphism; overburden compaction scheme; drifting snow compaction.

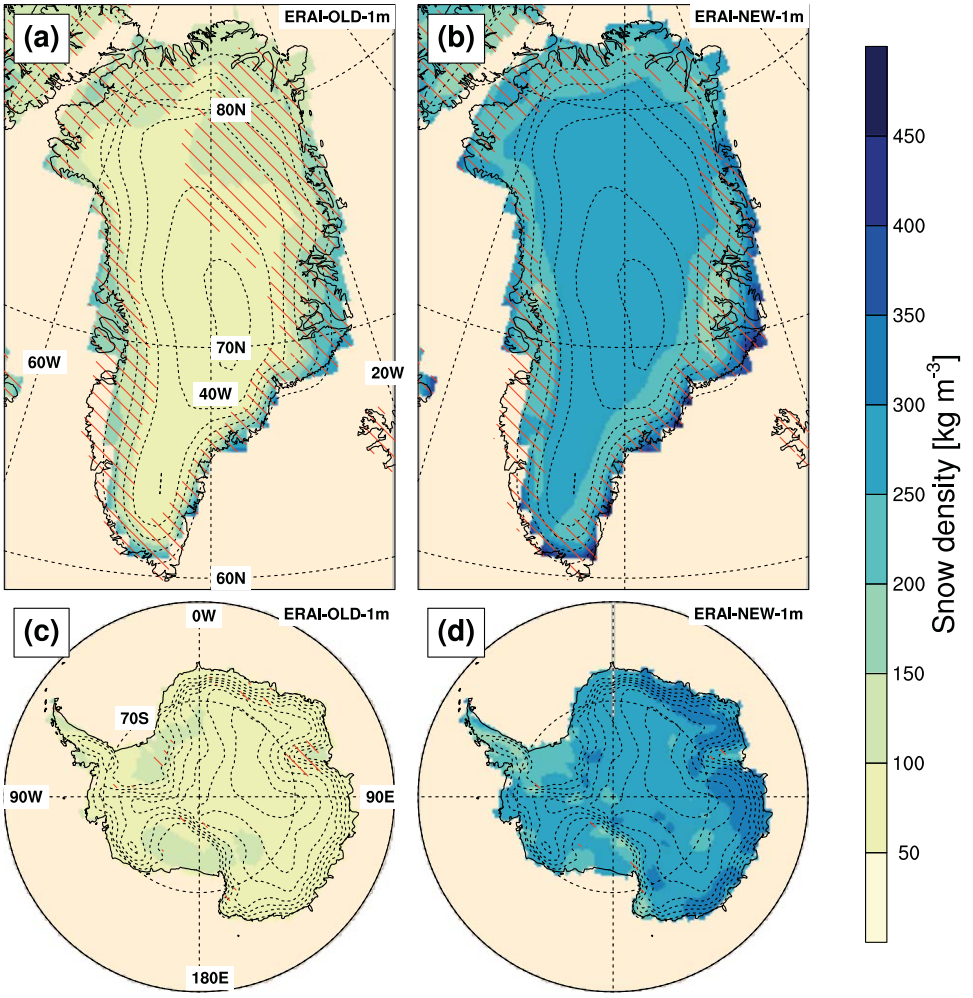

Figure 6. Annual mean density in the uppermost snow model layer (1979–1998) for (a, c) old model physics and (b, d) new model physics. Dotted lines represent 500 m elevation contours. Dashed areas become snow-free at least once during the averaging period, which could bias the displayed annual density value away from the summer value. Note that the uppermost snow model layer has variable depth, with a minimum and maximum thickness of 1 and 3 cm, respectively (Table 2). In case of a permanent deep snow cover, the layer thickness is approximately 2 cm.

Angelen et al., 2012). On the AIS, melt and refreezing now compare well to RACMO, but we cannot exclude the possibility of compensating errors.

The increase in snow depth in simulation ERAI-NEW-10m leads to significantly higher snow and ice temperatures. Figure 9 shows vertical profiles at a grid cell located in the West Greenland percolation zone, during four consecutive years. Thermal conductivity, shown in the top panels, is somewhat time dependent, yet does not vary greatly with depth, as density does not vary greatly with depth. Even with $H_{max} = 10$ m, the density profile is rather uniform because overburden pressure compaction is a relatively weak force. On the other hand, the sharp transition to ice density at zero height is clearly visible. Thermal heat flux exhibits a strong seasonal cycle in the shallow snow pack experiment (Figure 9c). Heat is conducted upward in winter, cooling the ice underneath the snow, with the reverse taking place in summer. With a deeper snow pack, this seasonal cycle changes in several aspects (Figure 9d). First, the enhanced insulating properties of the deeper snow pack now shield the glacial ice from the strong heat fluxes near the surface, seen as lighter colors below 0 m. Second, the pattern of heat transfer changes, with an overall stronger upward flux in winter and a weaker downward flux in summer. This is explained by the higher snow temperatures (Figures 9e and 9f), which strengthen vertical temperature gradients in winter and weaken them in summer. Finally, the deep snow pack allows refreezing to take place at much greater depths, thereby damping the

Table 5
Comparison of Integrated Melt, Refreezing and Runoff Fluxes Between ERA-Interim Forced CLM and Polar Regional Model RACMO Version 2.3

	ERAI-OLD-1m	ERAI-NEW-1m	ERAI-NEW-10m	RACMO2
GrIS μ (σ) in Gt yr^{-1}				
Melt	572 (141)	160 (49)	156 (48)	433 (68)
Refreezing	418 (98)	128 (35)	143 (36)	200 (27)
Runoff	173 (52)	53 (19)	36 (14)	265 (51)
AIS μ (σ) in Gt yr^{-1}				
Melt	913 (784)	105 (69)	100 (64)	94 (22)
Refreezing	770 (605)	88 (51)	92 (52)	91 (27)
Runoff	124 (90)	18 (10)	8 (3)	4 (2)

Note. Melt values represent the sum of ice and snow melt. For ERAI-CLM, the forcing period 1979–1998 was used and spatial integration was performed on the native CESM ice mask (GrIS area: 1,721,945 km^2, AIS area: 14,002,500 km^2). RACMO2 time averages span the period 1961–1990 (GrIS; van den Broeke et al., 2016) and 1979–1998 (AIS; Van Wessem et al., 2014), and native RACMO2 ice masks were used for the spatial integration (GrIS area: 1,718,736 km^2, AIS area: 13,926,689 km^2).

downward heat flux in summer. Refreezing continues well into autumn, with the highest snow temperatures seen in September and October, in contrast to the shallow snow pack where temperature peaks already in July. The deeper meltwater percolation, storage and refreezing is what causes the marked increase in (ice) temperature seen in the deeper snow pack configuration (Figure 9f). In the shallow pack configuration (Figure 9e), water percolating below H_{max} is sent to runoff, thereby removing latent heat from the pack. Additionally, heat released by refreezing in deeper model layers has a longer-lasting effect on the temperature profile compared to heat released close to the surface, since the overlying snow/firn acts as an insulator. At this particular site, we find that warming due to deeper percolation raises deep ice temperature by about 10°C.

To quantify how important the effect of deep percolation is on the ice temperature, we carried out a set of idealized experiments with the dry snow densification model described in section 4.1. The code was adapted in order to support (1) capping to a given H_{max}, (2) glacial ice layers (25 m in total) that permanently sit underneath the simulated snow pack, and (3) an external heat flux Q (J s^{-1}), that represents latent heat released through refreezing. Skin temperature is idealized as a sinoid, with a mean of 250°K and an amplitude of 10°K. A constant accumulation rate is assumed, with a total annual accumulation of 1,000 mm. Surface density is set to a constant value of 350 kg m^{-3} and the Herron and Langway (1980) dry densification rate is used. The (virtual) refreezing volume is varied between 50, 100, and 200 mm yr^{-1}, from which

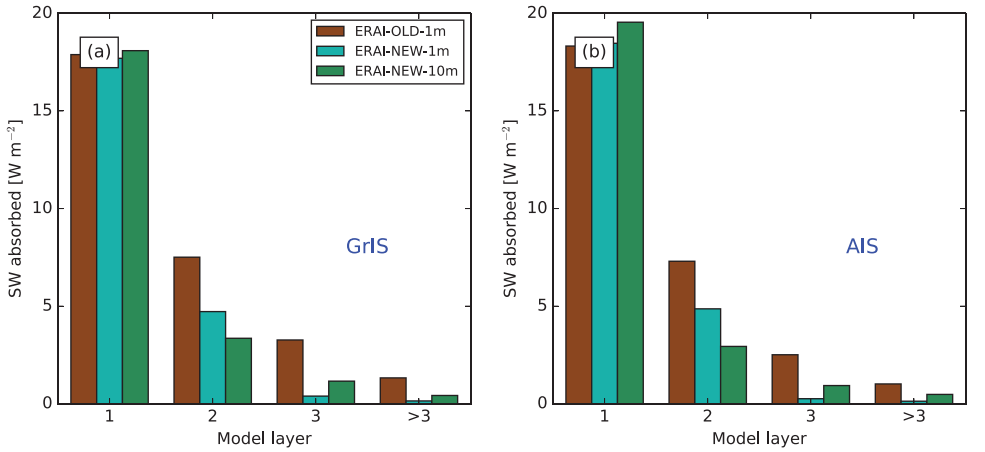

Figure 7. Mean annual absorbed shortwave radiation per model layer. Values represent area-averages over the time period 1979–1998. (a) GrIS and (b) AIS. Numbering of layers starts at the snow-atmosphere interface, increasing downward. Note that absorption rates are raw model output and have not been normalized for layer thickness.

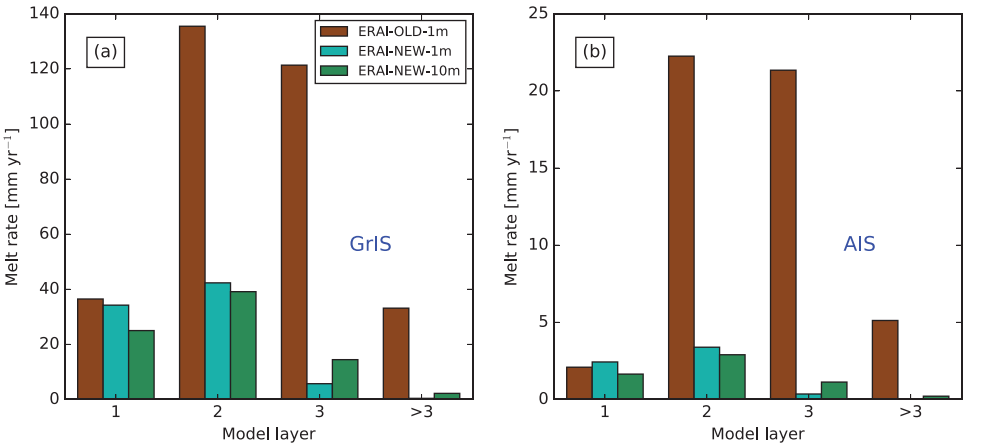

Figure 8. Melt rate distribution over individual model layers. Values represent area-averages over the time period 1979–1998. (a) GrIS and (b) AIS. Numbering of layers starts at the snow-atmosphere interface, increasing downward. Note that melt rates are raw model output and have not been normalized for layer thickness.

the external heat flux Q is calculated. Q is only applied for 90 days during summer and the simulation is run to equilibrium. First, we applied Q to just the top 1 m SWE, which represents the case that only shallow percolation and refreezing is allowed. We find that the difference in ice temperature at 25 m between the

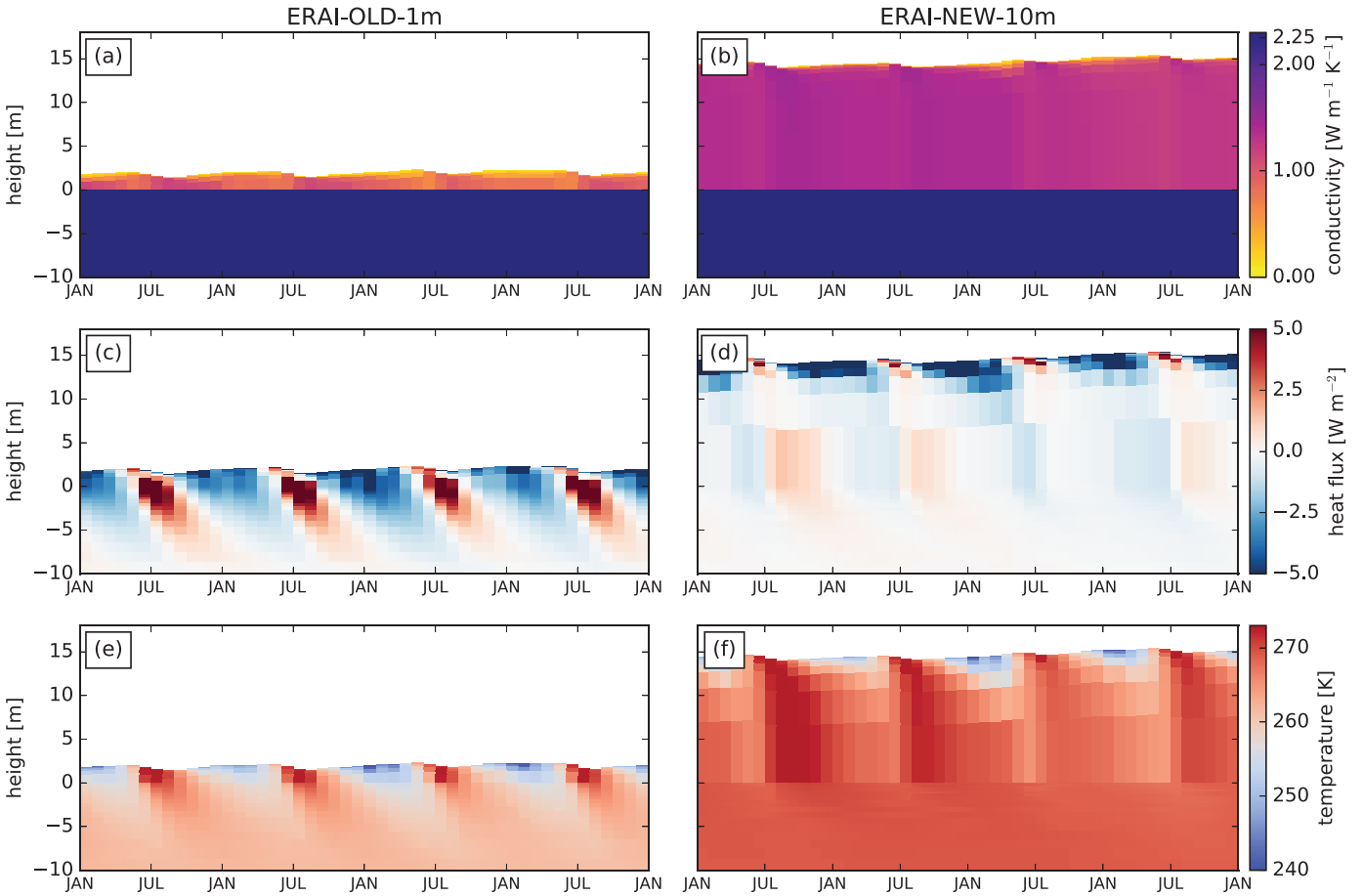

Figure 9. Vertical profiles at model grid point 67°23′N, 48°45′W, approximately along the Greenland K-transect, for the period 1983–1987. (a, b) Thermal conductivity, (c, d) heat flux, with positive values downward, and (e, f) temperature. Zero height corresponds to the snow-ice interface. Only the upper 10 m of ice are shown.

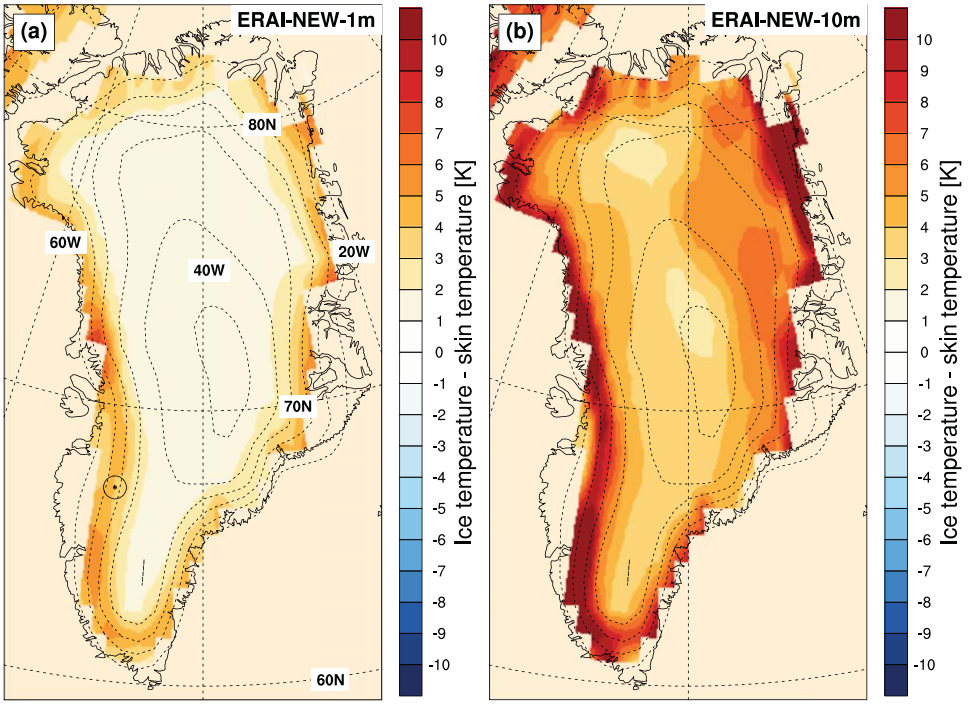

Figure 10. Mean annual difference of ice temperature minus skin temperature over the period 1979–1998, for simulations (a) ERAI-NEW-1m and (b) ERAI-NEW-10m. Ice temperature is taken equal to the uppermost soil layer. The marker in Figure 10a indicates the location of grid cell discussed in the text.

shallow ($H_{max} = 1$ m) and the deep ($H_{max} = 10$ m) snow pack is negligible for all three refreezing rates (<0.1°C). This suggests that the turnover rate of the snowpack, which is lower for greater H_{max}, by itself does not affect the equilibrium ice temperature. Next, we performed a set of experiments that allow for deep percolation and refreezing, i.e., Q is applied to the full snow pack depth H_{max}. Similar to the land-only CLM simulation, a net warming in the deep snow pack is observed. The virtual heat release of refreezing 50 mm yr^{-1} SWE raises deep ice temperature by 3.7°C relative to the shallow snow pack. This discrepancy increases dramatically in the medium (100 mm yr^{-1}) and high (200 mm yr^{-1}) refreezing scenarios, to 7.3 and 14.4°C, respectively. Yet stronger external forcings brought equilibrium ice temperatures above the melting point, which rendered these solutions nonphysical. We can conclude from these experiments that, in the presence of refreezing, percolation depth is a key determinant to the equilibrium deep ice temperature. Therefore, limiting snow depth by capping introduces a modeling error in many locations. In particular, ice temperature, used to force dynamical ice sheet models (Lipscomb et al., 2013), is underestimated.

Spatially, the deep ice warming due to additional latent heat release is present across the entire GrIS, yet most pronounced along the margins, where liquid water availability is greatest (Figure 10). The average GrIS difference between ice temperature and skin temperature, $T_{ice} - T_{skin}$, is 2.3°C for ERAI-NEW-1m, with a maximum of 6.7°C. Experiment ERAI-NEW-10m has an average $T_{ice} - T_{skin}$ value of 5.6°C and a maximum of 15.0°C, which matches the range that was indicated by the idealized experiments. The higher ice temperatures in the GrIS refreezing zones also agree with Meierbachtol et al. (2015), who found that 10 m snow temperatures may exceed surface temperature by up to 15°C in West Greenland.

To summarize, modeled ρ_{skin} increases virtually everywhere over the ice sheets, due to the introduction of wind-dependent fresh snow density (section 3.3), a wider destructive metamorphism range (section 3.4), and drifting snow compaction (section 3.5). The resulting snow densities are in line with other studies; for instance, Groot Zwaaftink et al. (2013) report deposited snow densities ranging from 250 to 450 kg m^{-3} at a site on the Antarctic Plateau. Surface density plays an important role in the production of subsurface melt through its direct link to thermal conductivity. The proposed model changes alleviate the excessive melt rates over the Antarctic (Lenaerts et al., 2016), provided that the atmospheric forcing is realistic. In our offline simulations, Greenland melt rates are underestimated, which is attributed to biases in the forcing data

and outstanding model biases that relate to melt. These biases will be investigated in follow-up work. The deeper snow pack led to a net increase in refreezing volume, and increased percolation depth was shown to cause a substantial warming of (deep) ice. The increase of H_{max} to 10 m SWE is a step in the right direction, but does not fully resolve firn processes, given that firn may grow up to tens of meters SWE in reality.

6. Conclusions

We presented a number of model improvements that enable a more realistic representation of polar firn and snow in CLM, while still providing realistic results for seasonal snow. The improvements have been tested using a series of offline dry firn densification experiments and were favorably compared to in situ data. The presented changes have recently been incorporated in the CLM codebase and will thus be standard in the next official release of CESM.

1. We resolved a conceptual design issue in the snow capping code that led to surface density occasionally becoming unrealistically high when H_{max} was reached.
2. We remedied the underestimation of surface snow density over ice sheets by the introduction of (1) a wind-dependent fresh snow density parametrization, (2) a higher maximum to the destructive metamorphism process, and (3) the introduction of compaction by drifting snow. With respect to a control run, we showed that these updates yield an improved simulation of near-surface density, a reduction in melt volume and a vertical redistribution of melt.
3. We replaced the overburden compaction scheme by an expression from Vionnet et al. (2012), showing greater skill in predicting firn density at depth. This update is relevant to the vertically integrated air content of the firn, or pore space, which partly determines refreezing capacity.
4. We increased the maximum modeled snow depth to $H_{max} = 10$ m SWE, which better approximates actual firn depth on ice sheets. The selected new maximum depth is a trade-off between a more realistic representation of total pore space, which acts as insulation for heat transfer and buffer for meltwater, and efficient spin-up of the snow pack in coupled model runs. Deeper percolation depths were found to raise snow and ice temperatures by several degrees. These findings are relevant to coupled ice sheet-climate models, since SMB and ice temperature are key boundary conditions for ice sheet models.

We intend to carry out a more complete analysis of CESM 2.0 ice sheet climate as soon as this new model version has been released. This explains why we have not analyzed the snow-atmosphere energy balance in the present paper. Further development of the CLM snow model could focus on one or more of the following topics: (1) the effect of vertical resolution on the thermal and hydrological state, (2) the adoption of a Lagrangian layering scheme in order to capture annual ice layers, (3) the introduction of grain shape parameters for modeling metamorphism, or (4) improving the pore close-off depth simulation. The latter would need particular attention were density to be used for predicting glacial inception. In future runs where the ice sheet is interactively coupled to the atmosphere, the lower Neumann boundary condition may be replaced by time-varying ice sheet temperature, to allow more realistic long-term transient runs.

Acknowledgments
This study is dedicated to the memory of Andrew Slater. The data used are listed in the references, and model code of the standalone dry firn model is available at https://github.com/lvankampenhout/compaction. Part of this study was funded by Utrecht University through its strategic theme Sustainability, subtheme Water, Climate & Ecosystems. Part of this work was carried out under the program of the Netherlands Earth System Science Centre (NESSC), financially supported by the Dutch Ministry of Education, Culture and Science (OCW). J.T.M.L. was supported by NWO ALW through a Veni postdoctoral grant 863.14.009. W.H.L. was supported by the Regional and Global Climate Modeling and Earth System Modeling programs of the Office of Biological and Environmental Research within the US Department of Energy's Office of Science. CESM simulations were supported by resources at the National Center for Atmospheric Research, Boulder, CO (NCAR/CISL). NCAR is sponsored by the National Science Foundation.

References

Anderson, E. A. (1976). *A point energy and mass balance model of a snow cover* (NOAA Tech. Rep. NWS 19). Silver Spring, MD: NOAA National Weather Service.

Arthern, R. J., Vaughan, D. G., Rankin, A. M., Mulvaney, R., & Thomas, E. R. (2010). In situ measurements of Antarctic snow compaction compared with predictions of models. *Journal of Geophysical Research*, *115*, F03011. https://doi.org/10.1029/2009JF001306

Arthern, R. J., Winebrenner, D. P., & Vaughan, D. G. (2006). Antarctic snow accumulation mapped using polarization of 4.3-cm wavelength microwave emission. *Journal of Geophysical Research*, *111*, D06107. https://doi.org/10.1029/2004JD005667

Benson, C. S. (1962). *Stratigraphic studies in the snow and firn of the Greenland ice sheet* (Tech. Rep. RR70). Hanover, NH: US Cold Regions Research and Engineering Laboratory.

Bougamont, M., Bamber, J. L., Ridley, J. K., Gladstone, R. M., Greuell, W., Hanna, E., . . . Rutt, I. (2007). Impact of model physics on estimating the surface mass balance of the Greenland ice sheet. *Geophysical Research Letters*, *34*, L17501. https://doi.org/10.1029/2007GL030700

Bromwich, D. H., Nicolas, J. P., & Monaghan, A. J. (2011). An assessment of precipitation changes over Antarctica and the Southern Ocean since 1989 in contemporary global reanalyses. *Journal of Climate*, *24*(16), 4189–4209. https://doi.org/10.1175/2011JCLI4074.1

Brun, E., Martin, E., & Spiridonov, V. (1997). Coupling a multi-layered snow model with a GCM. *Annals of Glaciology*, *25*, 66–72. https://doi.org/10.1017/S0260305500013811

Brun, E., Six, D., Picard, G., Vionnet, V., Arnaud, L., Bazile, E., . . . Seity, Y. (2011). Snow/atmosphere coupled simulation at Dome C, Antarctica. *Journal of Glaciology*, *57*(204), 721–736.

Church, J. A., Clark, P. U., Cazenave, A., Gregory, J. M., Jevrejeva, S., Levermann, A., . . . Nunn, P. D. (2013). Sea level change. In *Climate change 2013: The physical science basis. Contribution of Working Group I to the fifth assessment report of the Intergovernmental Panel on Climate Change* (pp. 1137–1216). New York, NY: Cambridge University Press.

Cullather, R. I., Nowicki, S. M. J., Zhao, B., & Suarez, M. J. (2014). Evaluation of the surface representation of the Greenland ice sheet in a general circulation model. *Journal of Climate*, *27*(13), 4835–4856. https://doi.org/10.1175/JCLI-D-13-00635.1

Dee, D. P., Uppala, S. M., Simmons, A. J., Berrisford, P., Poli, P., Kobayashi, S., . . . Vitart, F. (2011). The ERA-Interim reanalysis: Configuration and performance of the data assimilation system. *Quarterly Journal of the Royal Meteorological Society*, *137*(656), 553–597. https://doi.org/10.1002/qj.828

Fernandoy, F., Meyer, H., Oerter, H., Wilhelms, F., Graf, W., & Schwander, J. (2010). Temporal and spatial variation of stable-isotope ratios and accumulation rates in the hinterland of Neumayer station, East Antarctica. *Journal of Glaciology*, *56*(198), 673–687. https://doi.org/10.3189/002214310793146296

Flanner, M. G., & Zender, C. S. (2006). Linking snowpack microphysics and albedo evolution. *Journal of Geophysical Research*, *111*, D12208. https://doi.org/10.1029/2005JD006834

Goelzer, H., Huybrechts, P., Fürst, J. J., Nick, F. M., Andersen, M. L., Edwards, T. L., . . . Shannon, S. (2013). Sensitivity of Greenland ice sheet projections to model formulations. *Journal of Glaciology*, *59*(216), 733–749. https://doi.org/10.3189/2013JoG12J182

Graf, W., & Oerter, H. (2006). *High resolution density, conductivity, deuterium, and d18O of ice core FRI09C90_13*. PANGAEA. https://doi.org/10.1594/PANGAEA.548743

Groot Zwaaftink, C. D., Cagnati, A., Crepaz, A., Fierz, C., Macelloni, G., Valt, M., & Lehning, M. (2013). Event-driven deposition of snow on the Antarctic Plateau: Analyzing field measurements with SNOWPACK. *The Cryosphere*, *7*(1), 333–347. https://doi.org/10.5194/tc-7-333-2013

Guyomarc'h, G., & Mérindol, L. (1998). Validation of an application for forecasting blowing snow. *Annals of Glaciology*, *26*(1), 138–143. https://doi.org/10.3189/1998AoG26-1-138-143

Helsen, M. M., van de Berg, W. J., van de Wal, R. S. W., van den Broeke, M. R., & Oerlemans, J. (2013). Coupled regional climate–ice-sheet simulation shows limited Greenland ice loss during the Eemian. *Climate of the Past*, *9*(4), 1773–1788. https://doi.org/10.5194/cp-9-1773-2013

Helsen, M. M., Van Den Broeke, M. R., Van De Wal, R. S., Van De Berg, W. J., Van Meijgaard, E., Davis, C. H., . . . Goodwin, I. (2008). Elevation changes in Antarctica mainly determined by accumulation variability. *Science*, *320*(5883), 1626–1629.

Herron, M. M., & Langway, C. C. (1980). Firn densification: An empirical model. *Journal of Glaciology*, *25*(93), 373–385. https://doi.org/10.3189/S0022143000015239

Hu, A., Meehl, G. A., Han, W., & Yin, J. (2009). Transient response of the MOC and climate to potential melting of the Greenland Ice Sheet in the 21st century. *Geophysical Research Letters*, *36*, L10707. https://doi.org/10.1029/2009GL037998

Hunke, E. C., Lipscomb, W. H., Turner, A. K., Jeffery, N., & Elliott, S. (2010). *CICE: The Los Alamos Sea ice model documentation and software user's manual, version 4.1* (Rep. LA-CC-06–012). Los Alamos, NM: T-3 Fluid Dynamics Group, Los Alamos National Laboratory.

Hurrell, J. W., Holland, M. M., Gent, P. R., Ghan, S., Kay, J. E., Kushner, P. J., . . . Marshall, S. (2013). The Community Earth System Model: A framework for collaborative research. *Bulletin of the American Meteorological Society*, *94*(9), 1339–1360. https://doi.org/10.1175/BAMS-D-12-00121.1

Jordan, R. (1991). *A one-dimensional temperature model for a snow cover: Technical documentation for SNTHERM.89* (technical report). Hanover, NH: Cold Regions Research and Engineering Lab.

Kuipers Munneke, P., Ligtenberg, S. R. M., Noël, B. P. Y., Howat, I. M., Box, J. E., Mosley-Thompson, E., . . . van den Broeke, M. R. (2015). Elevation change of the Greenland Ice Sheet due to surface mass balance and firn processes, 1960–2014. *The Cryosphere*, *9*(6), 2009–2025. https://doi.org/10.5194/tc-9-2009-2015

Lamorey, G. W. (2003). *Simple shallow core density data*. Boulder, CO: National Snow and Ice Data Center. https://doi.org/10.7265/N52F7KCD

Lawrence, D. M., Oleson, K. W., Flanner, M. G., Thornton, P. E., Swenson, S. C., Lawrence, P. J., . . . Slater, A. G. (2011). Parameterization improvements and functional and structural advances in Version 4 of the Community Land Model. *Journal of Advances in Modeling Earth Systems*, *3*, M03001. https://doi.org/10.1029/2011MS00045

Lehning, M., Bartelt, P., Brown, B., Fierz, C., & Satyawali, P. (2002). A physical SNOWPACK model for the Swiss avalanche warning: Part II. *Snow Microstructure, Cold Regions Science and Technology*, *35*(3), 147–167.

Lenaerts, J. T., Vizcaino, M., Fyke, J., van Kampenhout, L., & van den Broeke, M. R. (2016). Present-day and future Antarctic ice sheet climate and surface mass balance in the Community Earth System Model. *Climate Dynamics*, *47*(5–6), 1367–1381.

Lenaerts, J. T. M., Le Bars, D., van Kampenhout, L., Vizcaino, M., Enderlin, E. M., & van den Broeke, M. R. (2015). Representing Greenland ice sheet freshwater fluxes in climate models. *Geophysical Research Letters*, *42*, 6373–6381. https://doi.org/10.1002/2015GL064738

Lenaerts, J. T. M., & van den Broeke, M. R. (2012). Modeling drifting snow in Antarctica with a regional climate model: 2. Results. *Journal of Geophysical Research*, *117*, M03001. https://doi.org/10.1029/2010JD015419

Li, J., & Zwally, H. J. (2004). Modeling the density variation in the shallow firn layer. *Annals of Glaciology*, *38*, 309–313. https://doi.org/10.3189/172756404781814988

Ligtenberg, S. R. M., Helsen, M. M., & van den Broeke, M. R. (2011). An improved semi-empirical model for the densification of Antarctic firn. *The Cryosphere*, *5*(4), 809–819. https://doi.org/10.5194/tc-5-809-2011

Lipscomb, W. H., Fyke, J. G., Vizcaíno, M., Sacks, W. J., Wolfe, J., Vertenstein, M., . . . Lawrence, D. M. (2013). Implementation and initial evaluation of the Glimmer Community Ice Sheet Model in the Community Earth System Model. *Journal of Climate*, *26*(19), 7352–7371. https://doi.org/10.1175/JCLI-D-12-00557.1

Liston, G. E., Haehnel, R. B., Sturm, M., Hiemstra, C. A., Berezovskaya, S., & Tabler, R. D. (2007). Simulating complex snow distributions in windy environments using SnowTran-3D. *Journal of Glaciology*, *53*(181), 241–256.

Machguth, H., MacFerrin, M., van As, D., Box, J. E., Charalampidis, C., Colgan, W., . . . van de Wal, R. S. W. (2016). Greenland meltwater storage in firn limited by near-surface ice formation. *Nature Climate Change*, *6*(4), 390–393. https://doi.org/10.1038/nclimate2899

Masson-Delmotte, V., Kageyama, M., Braconnot, P., Charbit, S., Krinner, G., Ritz, C., . . . Yu, Y. (2006). Past and future polar amplification of climate change: Climate model intercomparisons and ice-core constraints. *Climate Dynamics*, *26*(5), 513–529. https://doi.org/10.1007/s00382-005-0081-9

Meierbachtol, T. W., Harper, J. T., Johnson, J. V., Humphrey, N. F., & Brinkerhoff, D. J. (2015). Thermal boundary conditions on western Greenland: Observational constraints and impacts on the modeled thermomechanical state. *Journal of Geophysical Research: Earth Surface*, *120*, 623–636. https://doi.org/10.1002/2014JF003375

Mikolajewicz, U., Gröger, M., Maier-Reimer, E., Schurgers, G., Vizcaíno, M., & Winguth, A. M. E. (2007). Long-term effects of anthropogenic CO_2 emissions simulated with a complex earth system model. *Climate Dynamics*, *28*(6), 599–633. https://doi.org/10.1007/s00382-006-0204-y

Morris, E. M., & Wingham, D. J. (2011). The effect of fluctuations in surface density, accumulation and compaction on elevation change rates along the EGIG line, central Greenland. *Journal of Glaciology*, *57*(203), 416–430. https://doi.org/10.3189/002214311796905613

Mosley-Thompson, E., McConnell, J. R., Bales, R. C., Li, Z., Lin, P.-N., Steffen, K., . . . Bathke, D. (2001). Local to regional-scale variability of annual net accumulation on the Greenland ice sheet from PARCA cores. *Journal of Geophysical Research*, *106*(D24), 33839–33851. https://doi.org/10.1029/2001JD900067

Neale, R. B., Chen, C.-C., Gettelman, A., Lauritzen, P. H., Park, S., Williamson, D. L., . . . Lamarque, J.-F. (2010). *Description of the NCAR community atmosphere model (CAM 5.0)* (NCAR Tech. Note NCAR/TN-486+STR). Boulder, CO: National Center for Atmospheric Research.

Noël, B., van de Berg, W. J., Lhermitte, S., Wouters, B., Machguth, H., Howat, I., . . . van den Broeke, M. R. (2017). A tipping point in refreezing accelerates mass loss of Greenland's glaciers and ice caps. *Nature Communications*, *8*, 14730. https://doi.org/10.1038/ncomms14730

Noël, B., van de Berg, W. J., van Meijgaard, E., Kuipers Munneke, P., van de Wal, R. S. W., & van den Broeke, M. R. (2015). Evaluation of the updated regional climate model RACMO2.3: Summer snowfall impact on the Greenland Ice Sheet. *The Cryosphere*, *9*(5), 1831–1844. https://doi.org/10.5194/tc-9-1831-2015

Nowicki, S., Bindschadler, R. A., Abe-Ouchi, A., Aschwanden, A., Bueler, E., Choi, H., . . . Wang, W. L. (2013). Insights into spatial sensitivities of ice mass response to environmental change from the SeaRISE ice sheet modeling project II: Greenland. *Journal of Geophysical Research: Earth Surface*, *118*, 1025–1044. https://doi.org/10.1002/jgrf.20076

Nowicki, S. M. J., Payne, A., Larour, E., Seroussi, H., Goelzer, H., Lipscomb, W., . . . Shepherd, A. (2016). Ice Sheet Model Intercomparison Project (ISMIP6) contribution to CMIP6. *Geoscientific Model Development*, *9*(12), 4521–4545. https://doi.org/10.5194/gmd-9-4521-2016

Oerter, H., Wilhelms, F., Jung-Rothenhäusler, F., Göktas, F., Miller, H., Graf, W., & Sommer, S. (2000). Accumulation rates in Dronning Maud Land, Antarctica, as revealed by dielectric-profiling measurements of shallow firn cores. *Annals of Glaciology*, *30*, 27–34. https://doi.org/10.3189/172756400781820705

Oleson, K. W. (2013). *Technical description of version 4.5 of the Community Land Model (CLM)* (NCAR Tech. Note NCAR/TN-503+STR). Boulder, CO: National Center for Atmospheric Research.

Oleson, K. W., Lawrence, D. M., Bonan, G. B., Flanner, M. G., Kluzek, E., Lawrence, P. J., . . . Thornton, P. E. (2010). *Technical description of version 4.0 of the Community Land Model (CLM)* (NCAR Tech. Note NCAR/TN-478+STR). Boulder, CO: National Center for Atmospheric Research.

Oleson, K. W., Niu, G.-Y., Yang, Z.-L., Lawrence, D. M., Thornton, P. E., Lawrence, P. J., . . . Qian, T. (2008). Improvements to the Community Land Model and their impact on the hydrological cycle. *Journal of Geophysical Research*, *113*, G01021. https://doi.org/10.1029/2007JG000563

Pritchard, M. S., Bush, A. B. G., & Marshall, S. J. (2008). Neglecting ice-atmosphere interactions underestimates ice sheet melt in millennial-scale deglaciation simulations. *Geophysical Research Letters*, *35*, L01503. https://doi.org/10.1029/2007GL031738

Punge, H. J., Gallée, H., Kageyama, M., & Krinner, G. (2012). Modelling snow accumulation on Greenland in Eemian, glacial inception, and modern climates in a GCM. *Climate of the Past*, *8*, 1801–1819. https://doi.org/10.5194/cp-8-1801-2012

Rae, J. G. L., Aðalgeirsdóttir, G., Edwards, T. L., Fettweis, X., Gregory, J. M., Hewitt, H. T., . . . van den Broeke, M. R. (2012). Greenland ice sheet surface mass balance: Evaluating simulations and making projections with regional climate models. *The Cryosphere*, *6*(6), 1275–1294. https://doi.org/10.5194/tc-6-1275-2012

Ridley, J. K., Huybrechts, P., Gregory, J. M., & Lowe, J. A. (2005). Elimination of the Greenland Ice Sheet in a high CO_2 climate. *Journal of Climate*, *18*(17), 3409–3427. https://doi.org/10.1175/JCLI3482.1

Sato, T., Kosugi, K., Mochizuki, S., & Nemoto, M. (2008). Wind speed dependences of fracture and accumulation of snowflakes on snow surface. *Cold Regions Science and Technology*, *51*(2–3), 229–239. https://doi.org/10.1016/j.coldregions.2007.05.004

Smith, R., Jones, P., Briegleb, B., Bryan, F., Danabasoglu, G., Dennis, J., . . . Gent, P. (2010). *The Parallel Ocean Program (POP), reference manual, ocean component of the Community Climate System Model (CCSM) and Community Earth System Model (CESM)* (Rep. LAUR-01853, Vol. 141, pp. 1–140).

Swenson, S. C., & Lawrence, D. M. (2012). A new fractional snow-covered area parameterization for the Community Land Model and its effect on the surface energy balance. *Journal of Geophysical Research*, *117*, D21107. https://doi.org/10.1029/2012JD018178

van Angelen, J. H., Lenaerts, J. T. M., Lhermitte, S., Fettweis, X., Kuipers Munneke, P., van den Broeke, M. R., . . . Smeets, C. J. P. P. (2012). Sensitivity of Greenland Ice Sheet surface mass balance to surface albedo parameterization: A study with a regional climate model. *The Cryosphere*, *6*(5), 1175–1186. https://doi.org/10.5194/tc-6-1175-2012

van Angelen, J. H., Lenaerts, J. T. M., van den Broeke, M. R., Fettweis, X., & van Meijgaard, E. (2013). Rapid loss of firn pore space accelerates 21st century Greenland mass loss. *Geophysical Research Letters*, *40*, 2109–2113. https://doi.org/10.1002/grl.50490

van den Broeke, M. (2008). Depth and density of the Antarctic firn layer. *Arctic, Antarctic, and Alpine Research*, *40*(2), 432–438. https://doi.org/10.1657/1523-0430(07-021)[BROEKE]2.0.CO;2

van den Broeke, M. R., Enderlin, E. M., Howat, I. M., Kuipers Munneke, P., Noël, B. P. Y., van de Berg, W. J., . . . Wouters, B. (2016). On the recent contribution of the Greenland ice sheet to sea level change. *The Cryosphere*, *10*(5), 1933–1946. https://doi.org/10.5194/tc-10-1933-2016

van Pelt, W. J. J., Pohjola, V. A. & Reijmer, C. H. (2016). The changing impact of snow conditions and refreezing on the mass balance of an idealized Svalbard glacier. *Frontiers in Earth Science*, *4*, https://doi.org/10.3389/feart.2016.00102

Van Wessem, J., Reijmer, C., Morlighem, M., Mouginot, J., Rignot, E., Medley, B., . . . Van Meijgaard, E. (2014). Improved representation of East Antarctic surface mass balance in a regional atmospheric climate model. *Journal of Glaciology*, *60*(222), 761–770. https://doi.org/10.3189/2014JoG14J051

Vionnet, V., Brun, E., Morin, S., Boone, A., Faroux, S., Le Moigne, P., . . . Willemet, J.-M. (2012). The detailed snowpack scheme Crocus and its implementation in SURFEX v7.2. *Geoscientific Model Development*, *5*(3), 773–791. https://doi.org/10.5194/gmd-5-773-2012

Vizcaíno, M., Lipscomb, W. H., Sacks, W. J., van Angelen, J. H., Wouters, B., & van den Broeke, M. R. (2013). Greenland surface mass balance as simulated by the Community Earth System Model. Part I: Model evaluation and 1850–2005 results. *Journal of Climate*, *26*(20), 7793–7812. https://doi.org/10.1175/JCLI-D-12-00615.1

Vizcaíno, M., Mikolajewicz, U., Jungclaus, J., & Schurgers, G. (2010). Climate modification by future ice sheet changes and consequences for ice sheet mass balance. *Climate Dynamics*, *34*(2–3), 301–324. https://doi.org/10.1007/s00382-009-0591-y

Wagenbach, D., Graf, W., Minikin, A., Trefzer, U., Kipfstuhl, S., Oerter, H., & Blindow, N. (1994). *Annual means of density, d18O, deuterium, tritium, and accumulation rates of firn core BER01C90_01*. PANGAEA. https://doi.org/10.1594/PANGAEA.548637

Yen, Y.-C. (1981). *Review of thermal properties of snow, ice, and sea ice* (CRREL Rep. 81-10). Hanover, NH: Cold Regions Research and Engineering Lab.

Zhu, J., Liu, Z., Zhang, X., Eisenman, I., & Liu, W. (2014). Linear weakening of the AMOC in response to receding glacial ice sheets in CCSM3. *Geophysical Research Letters*, *41*, 6252–6258. https://doi.org/10.1002/2014GL060891